Optics & Laser Technology 200 (2026) 115094

Contents lists available at ScienceDirect

Optics and Laser Technology

journal homepage: www.elsevier.com/locate/optlastec

Full length article

Influence of laser beam shaping strategies on the microstructure and mechanical performance of aluminium to Hilumin dissimilar welds

Tianqiu Xu *, Ali Gökhan Demir

Department of Mechanical Engineering, Politecnico di Milano, Via La Masa 1, 20156 Milan, Italy

ARTICLE INFO

Keywords:
Beam shaping
Laser beam welding
Dissimilar materials
Battery pack
Busbar

ABSTRACT

With the rapid growth of electric vehicles (EV), ensuring reliable and efficient joining in battery packs has become increasingly critical, particularly for dissimilar materials such as aluminum busbars and Hilumin nickel-plated steel casings. This study aims to evaluate the feasibility and performance of laser beam welding (LBW) for aluminum busbars and Hilumin nickel-plated steel casings, with a particular emphasis on the role of beam shaping. In this work, LBW was systematically investigated under different beam-shaping configurations. The weldability window was established for various process conditions, and the resulting joints were characterized in terms of morphology, mechanical performance, and electrical resistance. The results demonstrate that beam shaping significantly influences weld formation and joint quality, with distinct effects observed at different welding speeds and power levels.Correlations between peak tensile force, electrical resistance, and weld cross-sectional area were identified, highlighting the importance of process optimization for improving joint reliability. Furthermore, the influence of intermetallic compounds (IMC) on the performance of dissimilar material joints under different beam-shaping conditions was analyzed. These findings indicate that beam shaping enables the formation of more reliable dissimilar LBW joints. Overall, this work provides a technical foundation for the application of LBW in advanced battery pack manufacturing and contributes to enhancing the safety, performance, and durability of EV power systems.

1. Introduction

Laser beam welding (LBW) has emerged as a key joining technology in electric vehicle (EV) battery manufacturing due to its ability to deliver concentrated energy with high precision, limited thermal distortion, and high productivity [1,2]. Compared with ultrasonic welding [3,4], wire bonding [5,6], and resistance spot welding [7], LBW offers superior process flexibility and scalability, specially for the connection process of electric vehicle batteries. As shown in Fig. 1, the weld have to ensure partial penetration to avoid damaging the cell cap while still guaranteeing mechanical integrity and low electrical resistance. These attributes make LBW particularly attractive for large-scale battery pack assembly.

The increasing demand for lightweight and high-performance batteries has intensified interest in aluminium busbars. However, in practical applications they are frequently joined to steel-based casings such as Hilumin, Hilumin is the trade name for a particular nickel-plated steel produced by TATA Steel, which is a nickel-plated low-carbon steel widely used in cylindrical and prismatic cells due to its corrosion resistance, malleability, and cost-effectiveness [8]. Despite its advantages in forming and corrosion resistance, Hilumin presents significant challenges when welded to aluminium due to differences in thermal conductivity, reflectivity, and metallurgical compatibility [9]. Prior studies have investigated approaches such as beam oscillation, surface modification, or interlayers to mitigate intermetallic compound (IMC) formation [10], while other works have explored the influence of interfacial microstructure on joint behaviour [11–15]. Nevertheless, how the spatial distribution of laser energy (particularly through beam-shaping control) governs melt pool behaviour and IMC evolution in aluminium–Hilumin joints is still not clearly understood. This knowledge gap limits the ability to design stable, high-quality welds for battery pack applications.

Building upon this motivation, recent advances in multi-core fibre lasers have introduced in-source spatial beam shaping as a promising tool to address these challenges [16]. By redistributing the laser power among core and ring beams, beam shaping enables deliberate tailoring of irradiance profiles and, consequently, the thermal field, melt-pool geometry, and interfacial mixing behaviour [17–21]. Although several

* Corresponding author.
E-mail address: tianqiu.xu@polimi.it (T. Xu).

https://doi.org/10.1016/j.optlastec.2026.115094
Received 19 December 2025; Received in revised form 16 February 2026; Accepted 7 March 2026
Available online 11 March 2026

studies have demonstrated the benefits of beam shaping in homogeneous or other dissimilar welding systems, such as improved stability, reduced porosity, and enhanced joint quality, its specific role in aluminium–Hilumin partial penetration welding has not been systematically explored [22,23]. In particular, it remains unclear how different power allocations influence IMC morphology, cross-sectional weld geometry, electrical resistance, and mechanical integrity, all of which are critical for EV battery manufacturing.

This study aims to fill this gap by experimentally evaluating the LBW process of aluminium busbars to Hilumin casings in cylindrical battery cells. A fiber laser with three coaxial cores was employed to investigate the effects of core/ring power distribution on weld formation, electrical resistance, and mechanical performance. The results provide a comprehensive assessment of process–property relationships and demonstrate how beam shaping can be leveraged to optimize joint quality. The weldability, electrical resistance, mechanical properties and Intermetallic compounds (IMC) distribution mechanism are experimentally analyzed. The findings are expected to contribute both to a deeper technical understanding of dissimilar laser welding of aluminium and Hilumin and to practical guidelines for improving the reliability and efficiency of EV battery pack manufacturing.

2. Materials and methods

2.1. Laser system

The experimental setup consists of a 5 kW fiber laser source with in-source beam-shaping capability (CFX-5000, nLIGHT, Vancouver, WA, USA). It also includes a scanner head equipped with a zoom module (Laser Processing Head MSH, Optoprim–Photonic Tools). The zoom module allows independent adjustment of the spot magnification. It also enables control of the spot position along the focal axis. The characteristics of the laser source used in the experiments are listed in Table 1. Fig. 2(a) illustrates the main components of the laser head and the optical chain. The laser processing head primarily includes the delivery fiber, zoom module, galvo scanner, f-theta lens, camera, and a secondary acquisition channel for monitoring purposes. The relationships among the various laser power components are shown in Fig. 2(a), where P_{tot} is the total laser power, P_{core} is the laser power of the core fiber, P_{ring1} is the laser power of the first ring fiber, P_{ring2} is the laser power of the second ring fiber.

The laser source provides 14 selectable power distributions, referred to as Beam Shapes (BS). Each beam shape delivers different power fractions to the three coaxial fibers, thereby producing distinct irradiance profiles. Among these beam shapes, BS0, BS3, and BS5 were selected as representative cases for analyzing the variation in power allocation across the three levels. The irradiance distributions of the different beam shapes at 1 kW are shown in Fig. 2(b), where xABS denotes the absolute position coordinate on the laser spot cross-section.

Table 1
Main specification of the laser system used in the experimental study.

Parameter	Value
Maximum power (kW)	5
Fiber core diameter (μm)	50
First ring diameter (μm)	175
Second ring diameter (μm)	330
Wavelength (nm)	1070 ± 10

2.2. Materials

In the experiments, the bottom plate was 0.2 mm thick Hilumin representing the battery casing material. The upper plate was 0.8 mm thick aluminium A1050, which represented the busbar. The nominal chemical composition of aluminium and Hilumin is shown in Table 2.

2.3. Experimental design

In this study, the experiments followed a logical sequence to highlight the progressivity of the research. As shown in Fig. 3, the flowchart of this study starts from determining the feasibility window for partial penetration welds, conducting experiments and identifying the key parameters, thereby further narrowing down the experimental scope and conducting characterization tests. Finally, based on the test results, the correlation is statistically analyzed to assist in explaining the mechanism of IMC formation in this LBW process.

2.3.1. Feasibility window

The experimental plan was designed to parametrically analyse the effect of the key process parameters namely power and speed along with the beam shape. The laser beam shapes and their power distributions used in the experiments are shown in Table 3. BS0 is the beam shape with the largest amount of power fed to the core fiber, it is consequently the beam closest to an ideal Gaussian beam. BS3 redirects 20% of the power from the core fiber to the two ring fibers. This results in a beam with a shape that is still very similar to a Gaussian beam, but with more than doubled the spot diameter and a reduction of the peak irradiance equal to reduction of power on the core fiber. The BS5 strongly tilts the power distribution towards the two coaxial fibers, reducing the amount of power delivered by the core fiber by a further 20% compared to BS3. Within the experiments the same core power (P_{core}) was used with

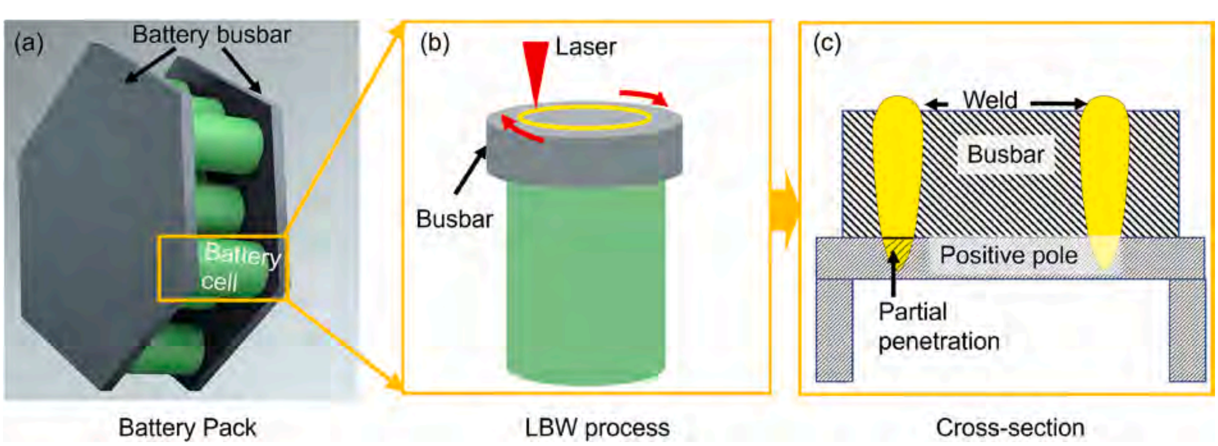

Fig. 1. Schematic diagram of dissimilar LBW about battery. (a) Description of battery pack. (b) Description of joint about battery cell and busbar by LBW. (c) LBW cross section of the partial penetration joint that connect busbar and battery cell.

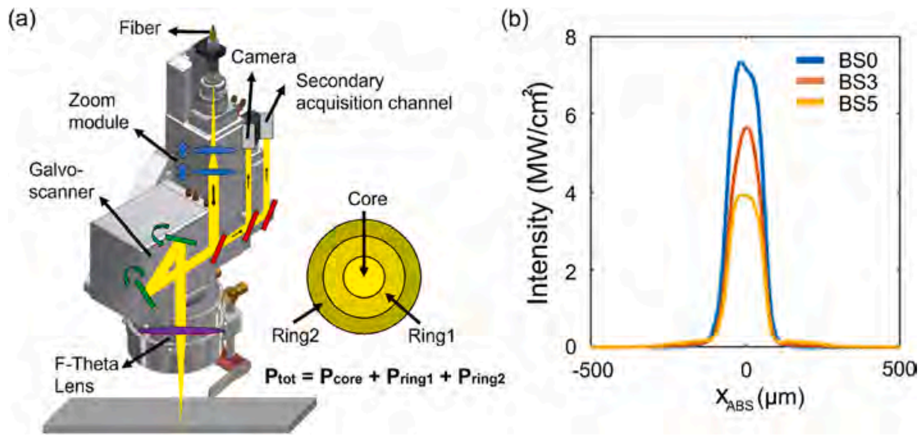

Fig. 2. (a) Fiber laser processing head used in the LBW experiment. (b) Irradiance of different BS at 1 kW total power.

Table 2
Nominal chemical composition of the aluminium A1050 and Hilumin.

Element (wt%)	Al	Si	Fe	Cu	Mg	Zn	C	Mn	S
A1050	Bal.	0.94	0.91	0.01	0.05	0.1			
Hilumin (base material)	0.07	0.02	Bal.				0.048	0.25	0.01

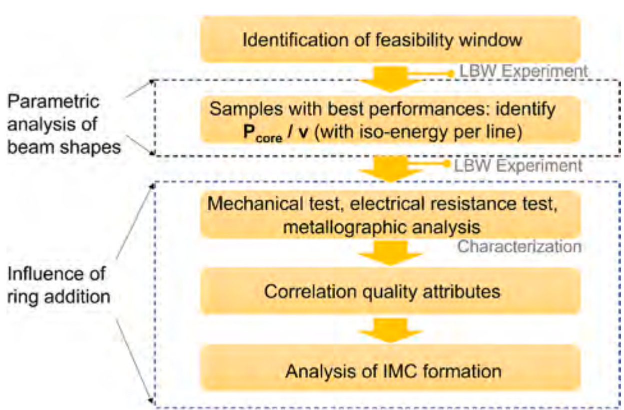

Fig. 3. Research flowchart for dissimilar LBW of aluminium to Hilumin.

Table 3
Beam shapes power distribution as declared by the laser source provider.

Beam shape	P_{core} (%)	P_{ring1} (%)	P_{ring2} (%)
BS0	92	3	4
BS3	71	13	16
BS5	50	33	17

different beam shapes to investigate the influence of the power added to ring. Fig. 4 illustrates the change in the power in the rings (P_{ring1}, P_{ring2}) and the total power (P_{tot}) as a function of the core power.

To determine the effectiveness of beam shaping in welding aluminium and Hilumin, it is first necessary to identify the parameter feasibility window within which the joint meets the minimum penetration requirements. The weld beads were classified in 3 different classes, fully penetrated, penetrated and not penetrated, as shown in Fig. 5. All conditions in which the energy supplied will not be sufficient to weld the two metals will be classified as not penetrated and excluded. Similarly, all conditions in which too much energy will be supplied, inducing full penetration of the lap joint, will also be discarded, that because it is not considered acceptable for the laser beam to come into contact with the electrolyte inside the cells due to safety reasons. Throughout the experiments a circular weld path with a diameter of 4 mm was employed. The list of all the levels of the fixed and variable parameters are exposed in Table 4.

2.3.2. *Laser weldability with iso-energy per line conditions*

Iso-energy per line conditions refer to selecting the most suitable process combination conditions based on the feasibility window, and conducting subsequent characterization studies based on this. Table 5 shows the P_{core}/v values for all process combinations in Table 4. After obtaining the feasibility window of the experiment, this study determined the $P_{core}/v = 2.88$ as the experimental condition for subsequent characterization and analysis. The list of all the fixed and variable parameters are shown in Table 6.

2.3.3. *Characterization of weld properties*

The characterization was performed only for partial weld conditions corresponding to the identified *iso*-energy per line cases. Among the six replications, all specimens were used for electrical resistance measurements. Five specimens were subjected to mechanical testing to evaluate the joint mechanical properties, while one specimen was reserved for metallographic analysis. As shown in Fig. 6(a), the welded specimens were first sectioned at the exact midpoint of the welding geometry using an abrasive saw and subsequently mounted in resin. Several geometric parameters related to the weld cross section were measured using image processing software (ImageJ). Fig. 6(a) illustrates the extracted geometric parameters, including the melt pool width at the top surface (W_1), the melt pool width at the root (W_2), and the total melt pool area (A_m). In addition, A_{mix} was defined as the percentage of dark regions observed in the metallographic cross-sectional images, serving as an indirect indicator of the mixing region between aluminium and iron and, consequently, of intermetallic compound (IMC) formation. The weld seam areas on the aluminium (A_{Al}) and on the Hilumin (A_{Hil}) were also quantified to assess the relative contribution of each material to the mixing process. After grinding and polishing, chemical etching was performed using Keller's reagent (2%), a solution commonly employed for aluminium alloys, consisting of 95% H_2O, 2.5% HNO_3, 1.5% HCl, and 1% HF. The final characterization stage involved microstructural observation using either an optical microscope or a scanning electron microscope (SEM).

To characterize the mechanical performance under different welding

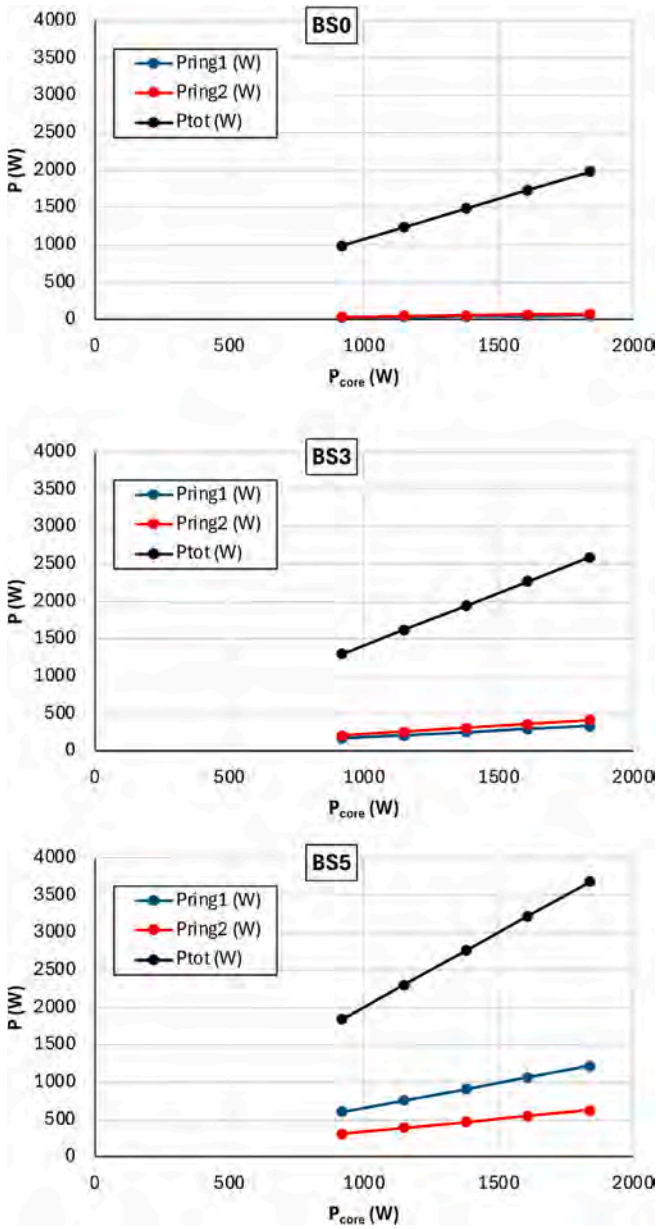

Fig. 4. Power distribution in the coaxial rings (P_{ring1}, P_{ring2}) and the total power (P_{tot}) as a function of the used power in the core (P_{core}) for the tested beam shapes (BS0, BS3, BS5).

conditions, tensile tests were conducted on lap-joint specimens to determine the maximum load sustained prior to fracture. Specimen preparation followed BS EN ISO 14273:201, as illustrated in Fig. 6(b). Tensile testing was carried out using a universal testing machine (MTS Synergie) with spring-loaded grips. The specimen dimensions are reported in Table 7 [24,25].

Electrical resistance measurements were performed using a four-wire measurement configuration with an imposed current of 3 A. To establish a reliable relationship between process parameters and electrical resistance, a highly precise measurement chain capable of resolving resistance variations below 0.1 mΩ was required. For each specimen, the resistance measurement was repeated 50 times, and the averaged value was used to minimize the influence of electrical interference and white noise. To ensure that only the weld region was characterized, thin insulating foils were inserted between the two edges of the lap joint, as shown in Fig. 6(c).

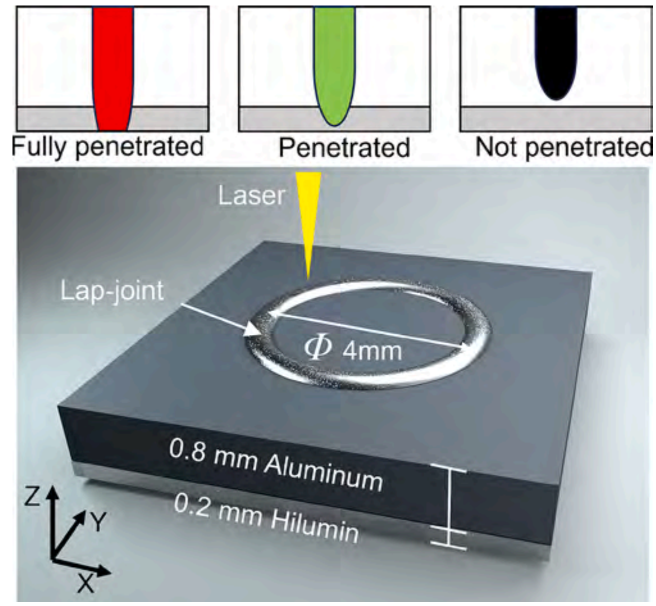

Fig. 5. Schematic diagram of LBW materials and paths as well as the 3 different classes of weld penetration.

Table 4
Experimental parameters in the experiment of feasible window.

Fixed parameters	Value
Wavelength (mm)	1070
Spot diameter (μm)	156
Defocus	0
Magnification	3.125
Variable parameters	**Value**
Speed, v (mm/s)	100, 250, 400, 550, 700
Core power, P_{core} (W)	920, 1150, 1380, 1610, 1840
Beam shapes, BS	BS0, BS3, BS5

Table 5
P_{core}/v value of all the process combinations (unit: J/mm).

P_{core} (W)	v (mm/s)				
	100	250	400	550	700
920	9.20	3.68	2.30	1.67	1.31
1150	11.50	4.60	2.88	2.09	1.64
1380	13.80	5.52	3.45	2.51	1.97
1610	16.10	6.44	4.03	2.93	2.30
1840	18.40	7.36	4.60	3.35	2.63

Table 6
Experimental parameters in the experiment of *iso*-energy per line conditions.

Fixed parameters	Value
Wavelength (mm)	1070
Spot diameter (μm)	156
Defocus	0
Iso-energy, P_{core}/v (J/mm)	2.88
Magnification	3.125
Variable parameters	**Value**
Core power, P_{core} (W)	1150, 1581, 2013
Speed, v (mm/s)	400, 550,700
Beam shapes, BS	BS0, BS3, BS5

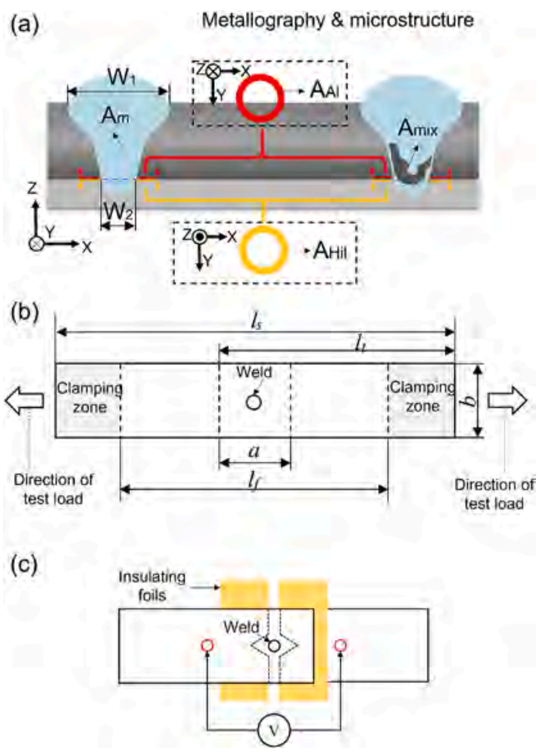

Fig. 6. (a) Metallographic characterization and measurement of LBW cross-sectional area (laser weldability samples with *iso*-energy per line conditions). (b) Mechanical resistance characterization of LBW samples (laser weldability samples with *iso*-energy per line conditions). (c) Electrical resistance characterization of LBW samples (laser weldability samples with *iso*-energy per line conditions).

Table 7
The size parameter of the specimens (as shown in Fig. 4(c)) used in mechanical resistance.

Thickness, t (mm)	Overlap, a (mm)	Width, b (mm)	Length of test piece, l_t (mm)	Total specimen length, l_s (mm)
0.2–0.8	30	30	90	150

3. Results and discussion

3.1. Feasibility window

Fig. 7 presents the optical microscopy images of all specimens produced on the two opposite sides of the lap joint, namely the top surface of the aluminium plate and the bottom surface of the Hilumin sheet. Conditions for which only the aluminium side is shown correspond to parameter sets where no penetration was achieved. Parameter combinations with the same core power level and higher welding speeds were omitted, as they would result in even lower penetration depths.

With increasing core power, the weld seams expand on both the top and bottom sides of the joint. Conversely, increasing the welding speed reduces the penetration depth, progressively shifting the welding regime from full penetration to partial penetration and ultimately to non-penetrated welds.

The influence of beam shape variation on weld bead dimensions is clearly observable on the top surface of the aluminium sheets. In contrast, variations in beam shape do not induce significant changes in bead size on the bottom surface of the Hilumin sheets. This observation is consistent with the hypothesis that weld penetration is primarily governed by the core power. Meanwhile, the power distributed in the ring predominantly affects the weld morphology on the top surface. In Fig. 8, *iso*-energy lines were plotted based on P_{core}/v values in Table 5. It can be seen that selecting $P_{core}/v = 2.88$ as the *iso*-energy condition represents an optimal and reasonable choice within the feasible window.

3.2. Influence of beam shape on weld properties in the iso-energy conditions

3.2.1. Penetration depth and weld area

Microscopic images were acquired for all specimens after tensile testing on both sides of the joint and along both weld edges. The images are presented in Fig. 9 together with the corresponding process parameters. By fixing the P_{core}/v, specimens with comparable weld penetration depths were obtained, and all parameter combinations fell within the process feasibility window.

Nevertheless, identical penetration was not achieved for all conditions. In particular, at low core power, the welding process exhibited instability, resulting in penetration depths that were only marginally sufficient to enter the feasibility window. This behavior further demonstrates the high level of complexity associated with this process and configuration, which requires careful parameter fine-tuning to achieve a controlled and reproducible weld depth. The joint area was quantified from the microscopic images presented here and subsequently correlated with the other quality attributes in Section 3.3.

Metallographic analysis was performed on one specimen for each parameter combination. Fig. 10 shows cross-sectional views of both sides of the weld after chemical etching. The etching process highlights iron-rich regions dissolved within the aluminium matrix, thereby enabling an assessment of the amount of molten material and the associated forces generated within the melt pool. It can be observed that, for some parameter sets, the weld cross sections do not fully penetrate the material. This behavior can be attributed to process instabilities that lead to localized regions with insufficient joint penetration.

It is worth noting that the melt pool morphology varies significantly with different laser beam power distribution configurations. Increasing the power delivered through the ring fiber results in a pronounced widening of the melt pool at the top surface of the joint. However, this widening does not propagate to the bottom of the joint; instead, it remains confined within an angle of approximately 45°. Furthermore, although the intensity profiles shown in Fig. 2(b) appear qualitatively similar, with all beam shapes exhibiting a Gaussian-like central peak, the quantitative energy partitioning between the core and the rings differs substantially among the configurations. As reported in Table 2, the core power fraction decreases from 92% in BS0 to 71% in BS3 and further to 50% in BS5, accompanied by a corresponding increase in the energy delivered through the rings. This redistribution lowers the peak intensity and broadens the effective heating zone.

As a consequence, despite their comparable normalized intensity profiles, the different beam shapes interact with the material in distinct ways. BS0 promotes deeper and narrower weld penetration. In contrast, BS3 and BS5 provide a more uniform heat input that stabilizes the melt pool, resulting in wider welds, smoother surface morphology.

3.2.2. Electrical resistance

Fig. 11(a) and (b) present the electrical resistance values as a function of the core power and the total laser power, respectively. The results fall within a relatively narrow variation range of approximately 10% between the best and worst conditions. Nevertheless, a clear dependence of the joint electrical resistance on the total power can be identified. Specifically, the electrical resistance increases with increasing laser power, which is contrary to the trend commonly reported in laser welding of similar materials [24]. Although the experiments were conducted under *iso*-energy core conditions, a slight increase in the weld cross-sectional area can still be observed with increasing power.

During welding, IMC are formed at the interface. These phases exhibit relatively high electrical resistivity, and their presence can lead to an increase in the overall electrical resistance of the joint despite the

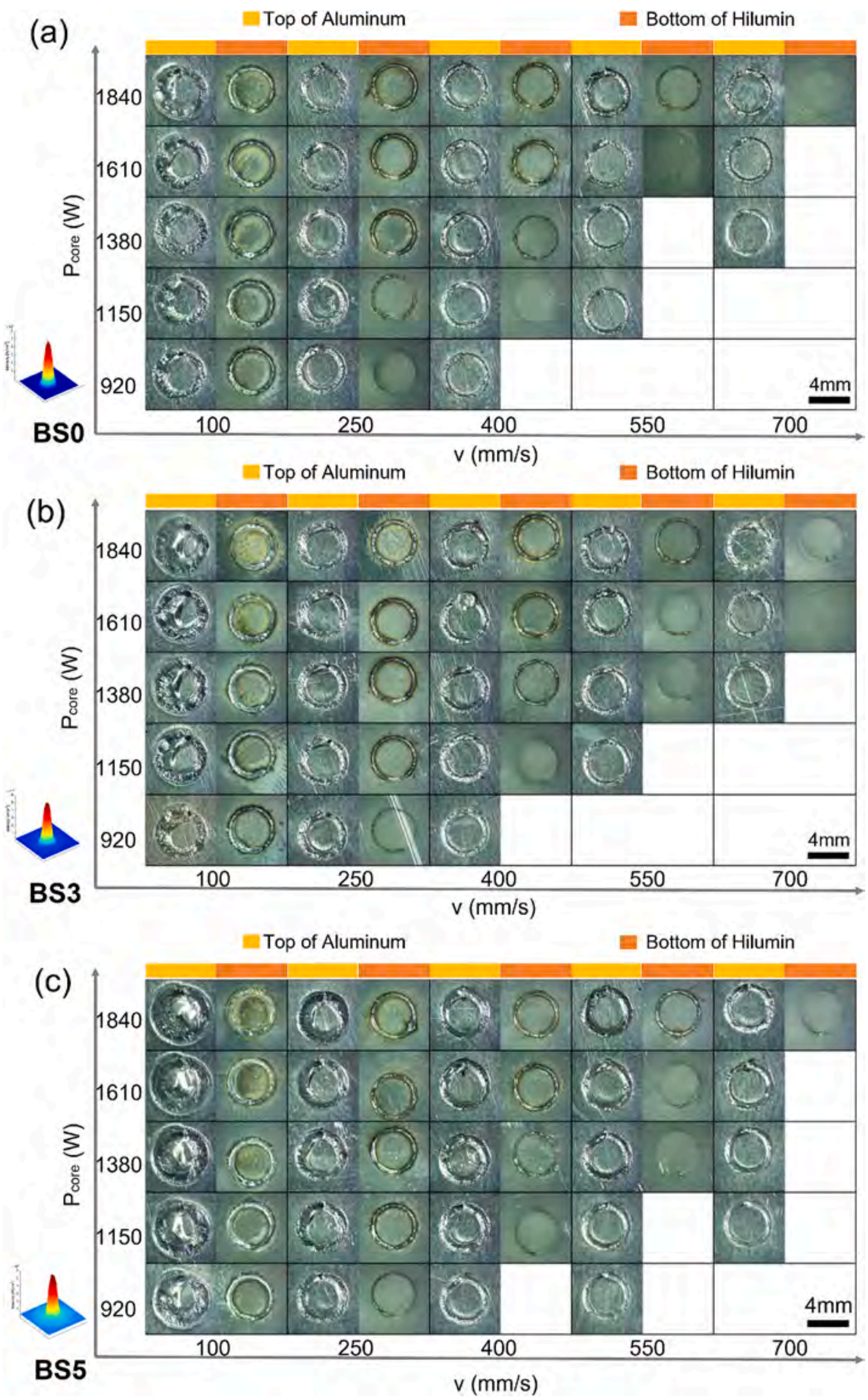

Fig. 7. Images of laser welded aluminium /Hilumin joints as a function of core power and weld speed using (a) BS0, (b) BS3, (c) BS5 beam shapes.

enlarged weld cross section. It is therefore reasonable to infer a strong correlation between IMC formation and the power level employed during welding.

In addition to weld microstructure and intermetallic compound (IMC) formation, the electrical performance of the joint can be significantly influenced by internal defects such as inclusions, porosity, and cracks. Non-metallic inclusions or intermetallic particles typically exhibit low electrical conductivity, thereby introducing localized regions of high resistance and disrupting uniform current flow.

Porosity reduces the effective cross-sectional area available for electrical conduction and may induce inhomogeneous current distribution, which in turn increases the overall electrical resistance of the joint. Cracks act as discontinuities in the conductive path; they not only impede or divert electron transport but also promote local current crowding, further degrading electrical conductivity and long-term stability.

3.2.3. *Mechanical resistance*

The load–displacement curves are presented in Fig. 12. The peak force at fracture (F_p) was extracted from the tensile curves and used as

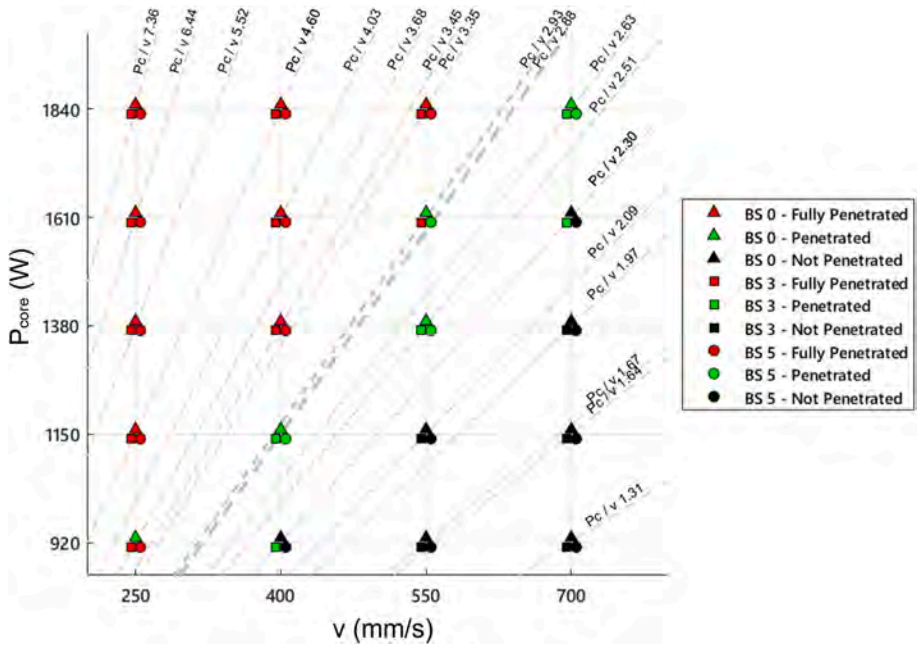

Fig. 8. Classification of the welded joints as a function of the penetration state, showing the feasibility window of partial penetration welds. The *iso*-energy per line P_{core}/v conditions are shown with dashed lines with the calculated values in J/mm.

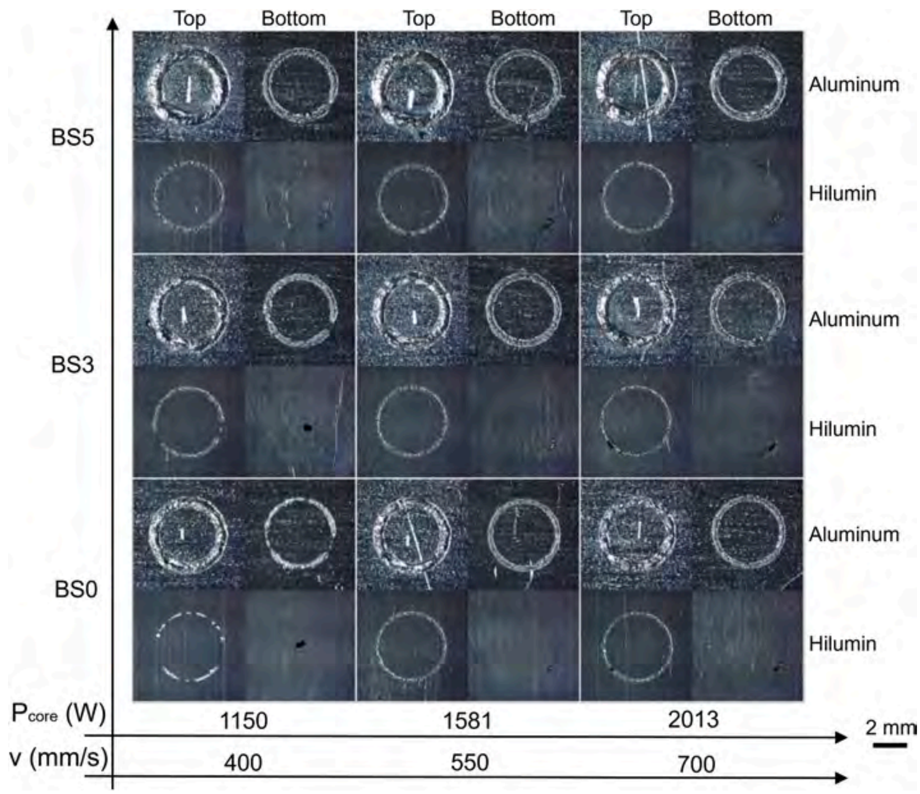

Fig. 9. Images of laser welded aluminium /Hilumin joints as a function of core power and weld speed using 2.88 J/mm energy per line.

an indicator of the mechanical performance of the joint. The results were averaged for each parameter set and are reported together with the corresponding error bars in Fig. 13. The three investigated beam shapes exhibit distinctly different trends in terms of peak fracture force. In addition, a substantial variation in the scatter of the results is observed among the different parameter combinations.

As shown in Fig. 13, for BS0, increasing the welding speed leads to a clear improvement in the mechanical properties of the joint. However, this improvement is accompanied by increased process instability, as evidenced by the large error bars. Compared with the Gaussian beam, the addition of power to the ring stabilizes the mechanical response of the joint. BS3 exhibits nearly constant mechanical properties and shows limited sensitivity to variations in process speed. Nevertheless, it is important to note that the variability of the results remains relatively

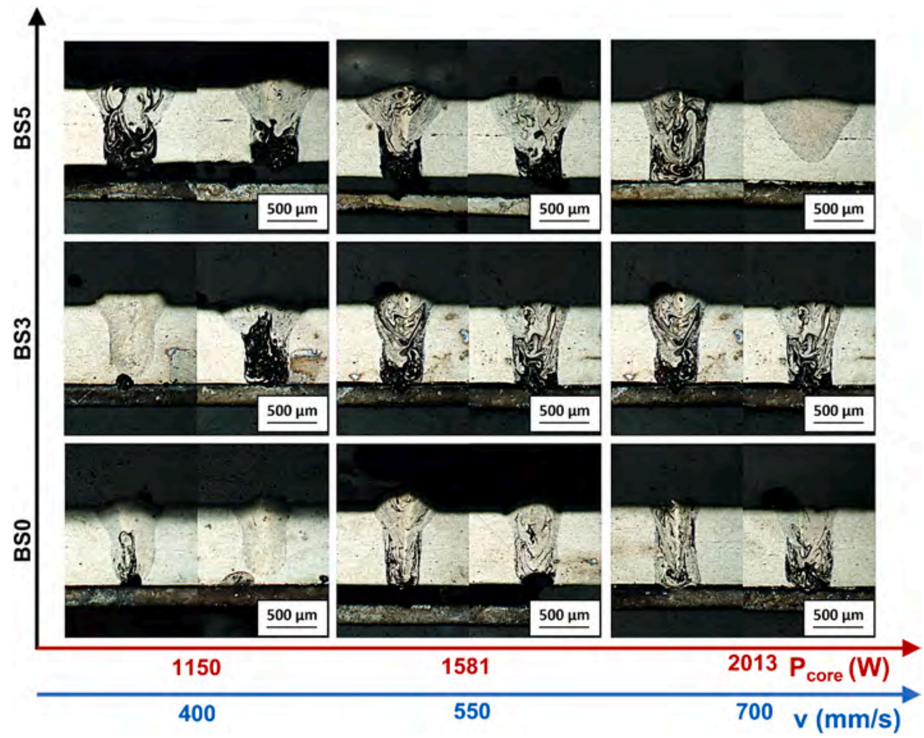

Fig. 10. Cross-section images of laser welded aluminium-Hilumin joints as a function of core power and weld speed using 2.88 J/mm energy per line.

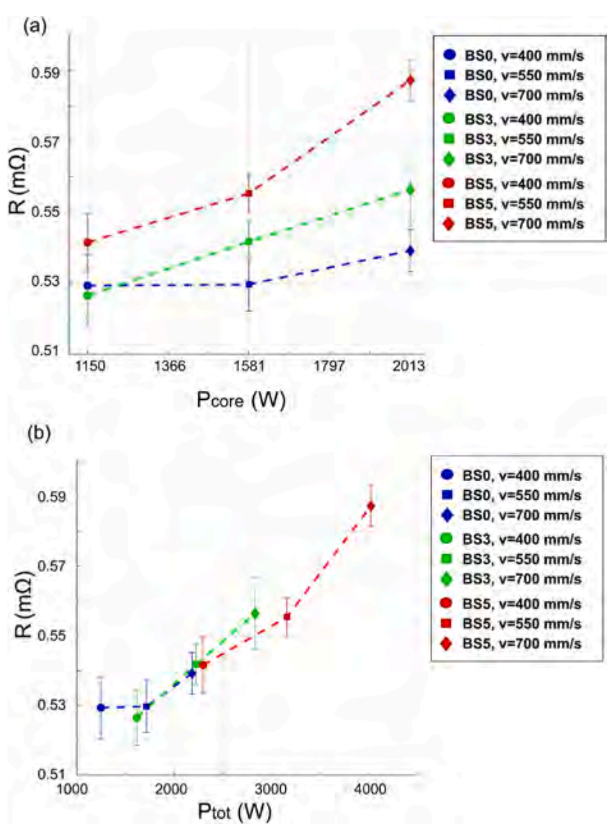

Fig. 11. (a) Average electrical resistance (R) as function of P_{core} and v with 2.88 J/mm energy per line. (b) Graph of average electrical resistance (R) as function of total power (P_{tot}).

high across all three investigated conditions.

BS5 displays an opposite trend compared with the Gaussian beam. In this case, a significant reduction in mechanical properties is observed as the process speed increases. At a welding speed of 400 mm/s, the highest mechanical performance and the lowest variability are achieved. In contrast, at higher speed levels, a pronounced degradation in mechanical properties is recorded. These results indicate that distributing a substantial fraction of the laser power (50%) to the ring is beneficial at low welding speeds, but becomes detrimental when the interaction time is reduced. This behavior can be attributed to enhanced nickel vaporization induced by higher local irradiance at increased process speeds.

3.2.4. Intermetallic compounds

To obtain a more detailed understanding of the formation and spatial distribution of IMC within the weld, SEM analysis was performed. This technique allows for the acquisition of high-magnification images and enables the reconstruction of both the chemical composition and the microstructure of the weld. As shown in Fig. 14, the SEM images are presented in greyscale, where lighter shades correspond to heavier elements and darker shades to lighter elements. This contrast is particularly evident in high-magnification images, where aluminium and Hilumin can be clearly distinguished outside the weld section. Regions exhibiting intermediate grey levels between these two extremes are therefore identified as intermetallic phases.

The morphology of the weld cross section varies substantially with the addition of power to the coaxial ring fiber, particularly affecting its shape and the distribution of intermetallics within the weld. It is observed that increasing the ring power enhances penetration under the analysed conditions. Consequently, while the P_{core}/v remains a primary factor in determining weld penetration depth, the total power employed also exerts a non-negligible influence. Nevertheless, as previously noted, the joint's mechanical properties do not correlate directly with penetration depth, as would be expected in welds of homogeneous materials; instead, they depend on the quantity, type, and distribution of IMC.

Increasing the power delivered to the ring fiber induces a pronounced widening of the weld near the top surface, with more limited effects near the root. The internal mixing within the weld also varies significantly with beam shape. A comparison of BS3 and BS5 cross

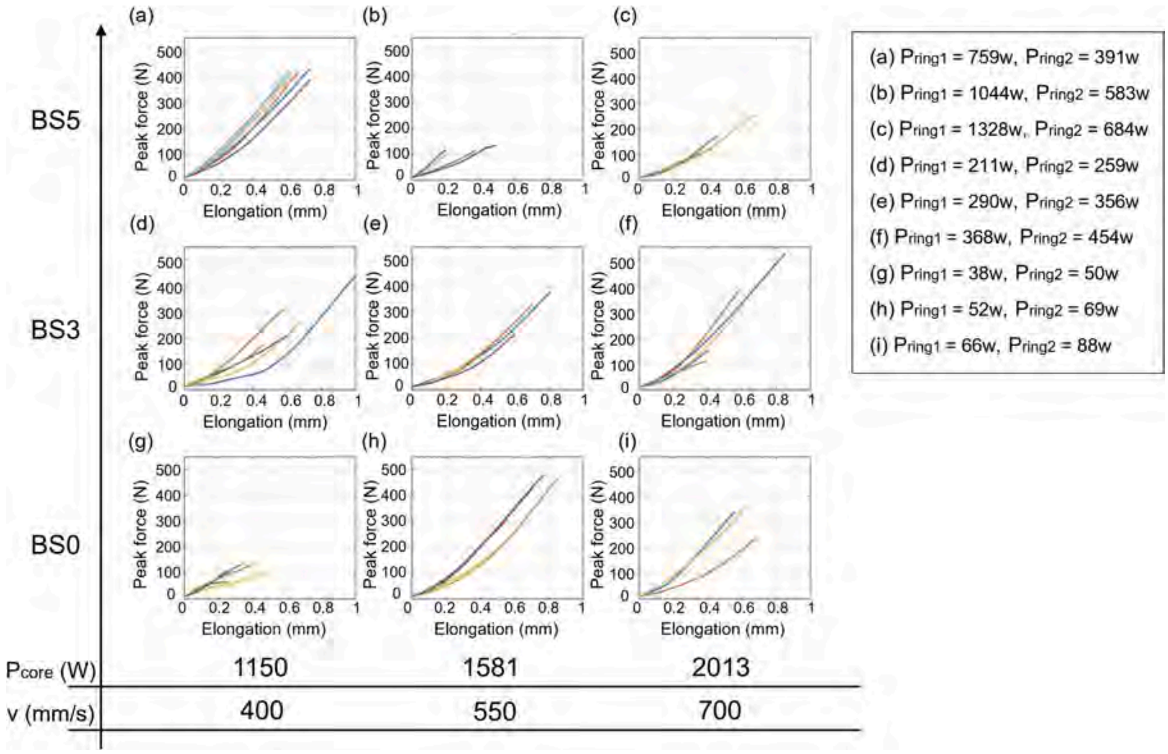

Fig. 12. Tensile test results as a function of core power, scan speed, and beam shape at the 2.88 J/mm energy per line.

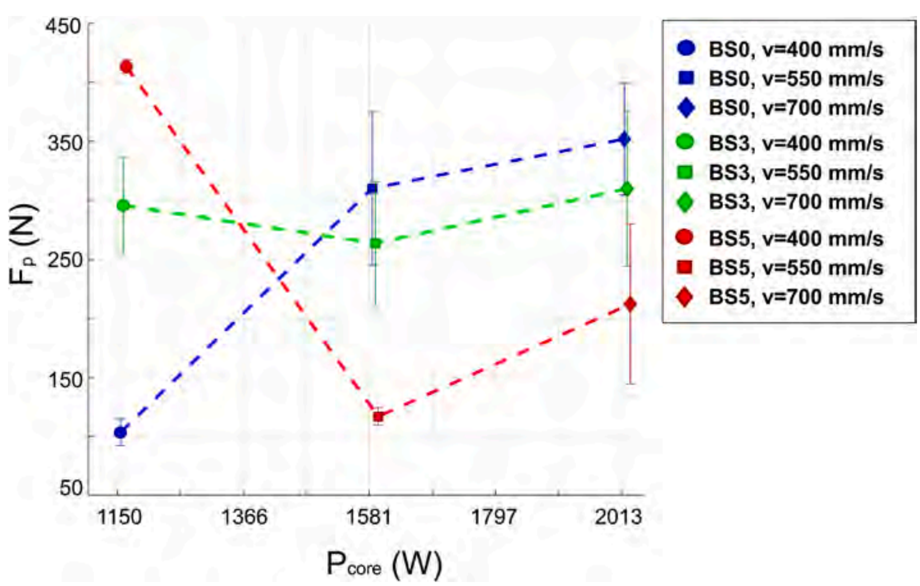

Fig. 13. Peak force at rupture as a function of the core power at the 2.88 J/mm energy per line in the experimented conditions.

sections is particularly illustrative: although the penetration into the Hilumin layer is nearly comparable, the IMC distribution differs markedly. In BS3, the IMC distribution is less compact, suggesting that the molten iron within the melt pool experiences stronger forces, causing upward migration. In contrast, for BS5, the IMC are concentrated near the lower portion of the weld close to the boundary. Furthermore, in-weld flows push the IMC towards the weld periphery in BS5, whereas for BS3, the intermetallic phases are primarily located at the seam center.

These observations indicate that variations in power distribution alter the forces within the melt pool, enhancing the effect of recoil pressure relative to buoyancy and Marangoni forces [26,27]. A more detailed analysis of the chemical composition of the intermetallic phases near the weld boundary was subsequently conducted using energy-dispersive X-ray spectroscopy (EDX). The results are presented in Fig. 15 and Table 8.

It should be noted that many of the phases identified during the EDX analysis contain a non-negligible amount of nickel. Concentrations exceeding 330 ppm have been found to significantly influence the formation and properties of intermetallic phases. Consequently, a simple Al–Fe binary analysis is no longer sufficient.

The predominant IMC in Al–Fe–Ni alloys is Al_9FeNi, whose mechanical properties differ substantially from the IMCs typically observed in Al–Fe welds, such as Al_5Fe_2 and $Al_{13}Fe_4$ [10,28]. For example, Site 6

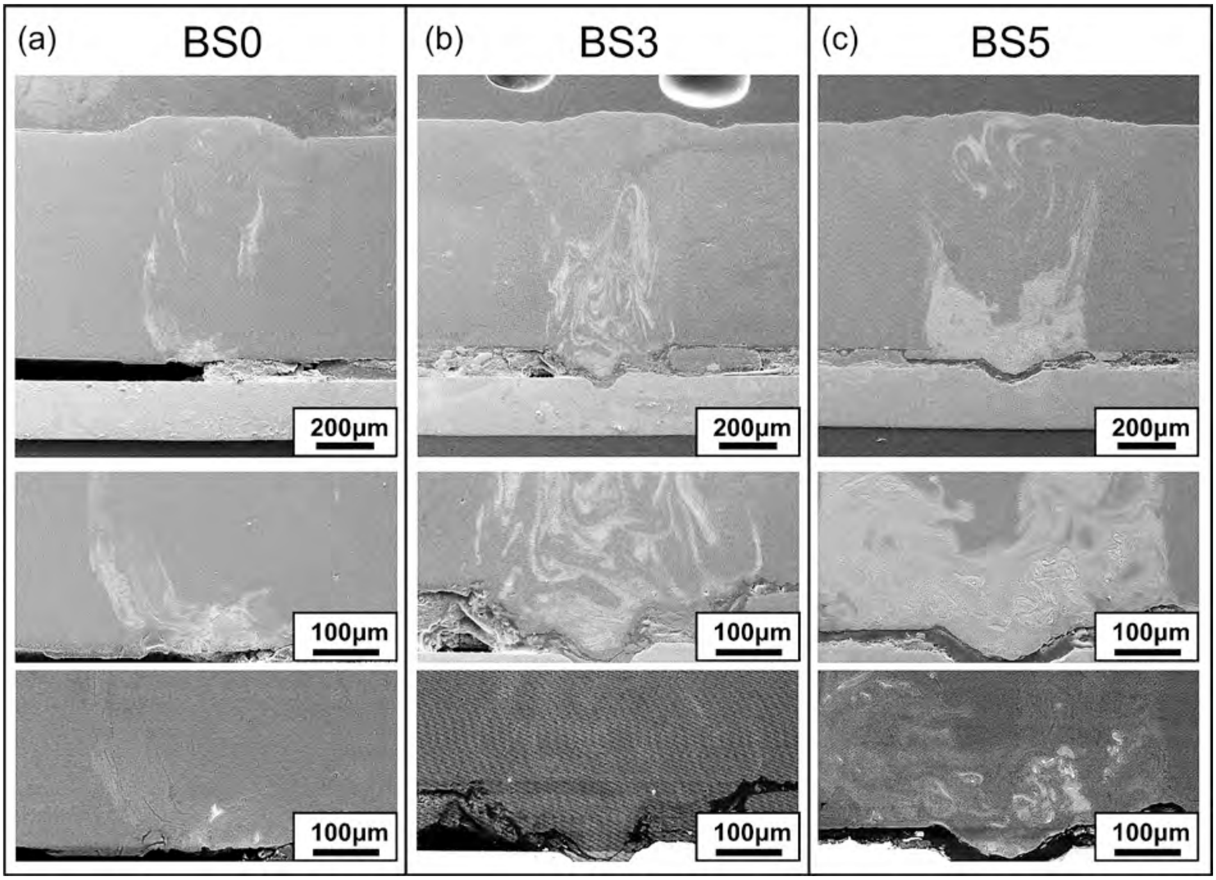

Fig. 14. SEM images of samples under the condition of P_{core} = 1150 W, v = 400 mm/s with different beam shapes. (a) BS0, (b) BS3, (c) BS5.

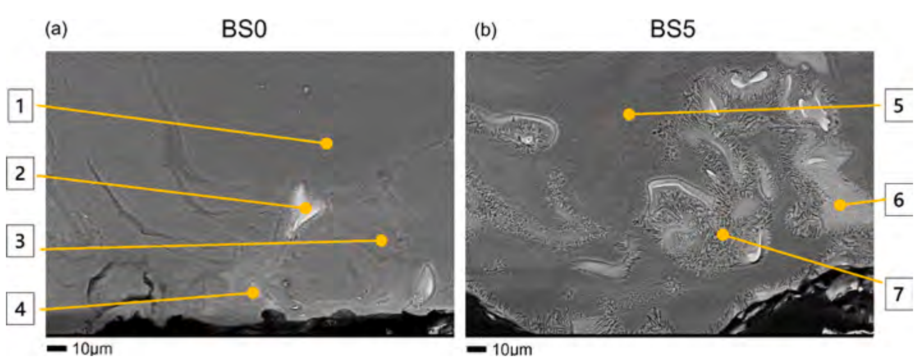

Fig. 15. EDX measurement points of weld joints produced using (a) BS0 (b) BS5 with P_{core} = 1150 W, v = 400 mm/s.

Table 8
EDX composition of IMC phases highlighted in Fig. 15.

Atomic Percent (At.) %	O	Al	Fe	Ni
1		100		
2		61.185	33.9	4.91
3		95.55	4.45	
4	9.83	73.96	12.74	3.47
5		97.78	2.22	
6		75.79	22.21	2.01
7		89.53	8.99	1.48

in Fig. 15 exhibits a chemical composition consistent with a mixture of 78% Al_5Fe_2 and 22% Al_9FeNi, while Site 7 shows a lamellar structure composed of 57% α-Al, 26% Al_5Fe_2 and 17% Al_9FeNi.

Further detailed analyses are required to verify that this reconstruction accurately reflects the actual chemical compositions of the phases present in the alloy. Nevertheless, the relatively high nickel content measured at the weld base likely contributes substantially to the mechanical strength of the joint. The sample welded with BS5 exhibits a more compact and condensed intermetallic layer at the weld base compared with BS3 and BS0, which promotes the formation of Ni-rich intermetallic phases near the weld section. Nickel has been shown to enhance the mechanical performance of Al–Fe intermetallics and reduce brittleness, thereby explaining the higher strength observed under this parameter set.

3.3. Correlation between the quality attributes

This section presents a comparison between the measured weld characteristics and the process variables. Weld geometry measurements were conducted optically as described in Section 2.3.3. Fig. 6(a) summarizes the geometry parameters obtained from the cross sections. Mechanical strength was evaluated based on the peak force (F_p) and the electrical resistance (R). All relevant process parameters were considered, particularly the laser scanning speed and the laser power, expressed in its various forms. The relationship between F_p and the welding cross-section geometric parameters, including the IMC area (A_{mix}), is presented in Fig. 16 based on the measurements in Fig. 10.

Table 9 presents the correlation matrix between process parameters and quality attributes, focusing on LBW weld geometry (e.g., fusion area on each substrate side), the extent of IMC formation, and the mechanical and electrical performance of the LBW joints. Analyzing the interrelations among these output parameters provides a deeper understanding of the mechanisms governing joint behavior in dissimilar metal welding.

The peak tensile force (F_p) exhibits a strong positive correlation with the weld bead area on the Hilumin side (A_{Hil}), with a correlation coefficient of 0.62, and a moderate positive correlation with the fusion area on the aluminum side (A_{Al}), with a coefficient of 0.51. Additionally, F_p shows a moderate positive correlation with the total IMC area (A_{mix}), with a correlation coefficient of 0.3. These results indicate that larger fusion zones on both the Hilumin and aluminum sides generally contribute to higher mechanical strength. Although excessive penetration into the Hilumin side is often thought to promote brittle IMC formation, which may reduce strength, the data suggest that within an appropriate range, adequate metallurgical bonding on both sides, including controlled IMC formation, can enhance joint structural integrity and mechanical performance.

In contrast, the electrical resistance (R) exhibits a moderate negative correlation with A_{Hil} (correlation coefficient −0.33), a strong negative correlation with A_{Al} and a strong positive correlation with A_{mix}. This implies that electrical resistance decreases as the aluminum-side fusion area increases, while larger IMC formation elevates resistance. Although Hilumin is designed for low contact resistance, excessive or poorly controlled fusion into this side may lead to insulating IMC or surface oxides, increasing resistance. Conversely, the high electrical conductivity and relatively low reactivity of aluminum favor the formation of a more conductive path, thereby reducing the overall resistance when sufficient aluminum fusion is achieved.

Overall, the data in Table 9 suggest that achieving balanced fusion between dissimilar materials is crucial for enhancing joint strength, while limiting IMC formation, particularly on the Hilumin side, is essential for maintaining low electrical resistance.

Table 9
Correlation Matrix of process parameters and quality attributes.

	W_1	W_2	A_m	A_{Hil}	A_{Al}	A_{mix}	F_p
W_2	0.61						
A_m	0.76	0.80					
A_{Hil}	−0.30	0.24	−0.08				
A_{Al}	−0.07	0.53	−0.09	0.56			
A_{mix}	0.51	0.57	0.47	−0.16	0.04		
F_p	−0.18	0.32	0.06	0.62	0.51	0.30	
R	0.51	0.67	0.48	−0.33	−0.68	0.54	−0.19

3.4. Effect of IMC on LBW characteristics

3.4.1. Formation mechanism of IMC

Based on the characterization phenomenon shown in Fig. 14, the formation of IMC under different BS is related to the fluid flow and force field changes in the melt pool [29]. Fig. 17 shows the fluid flow, forces,

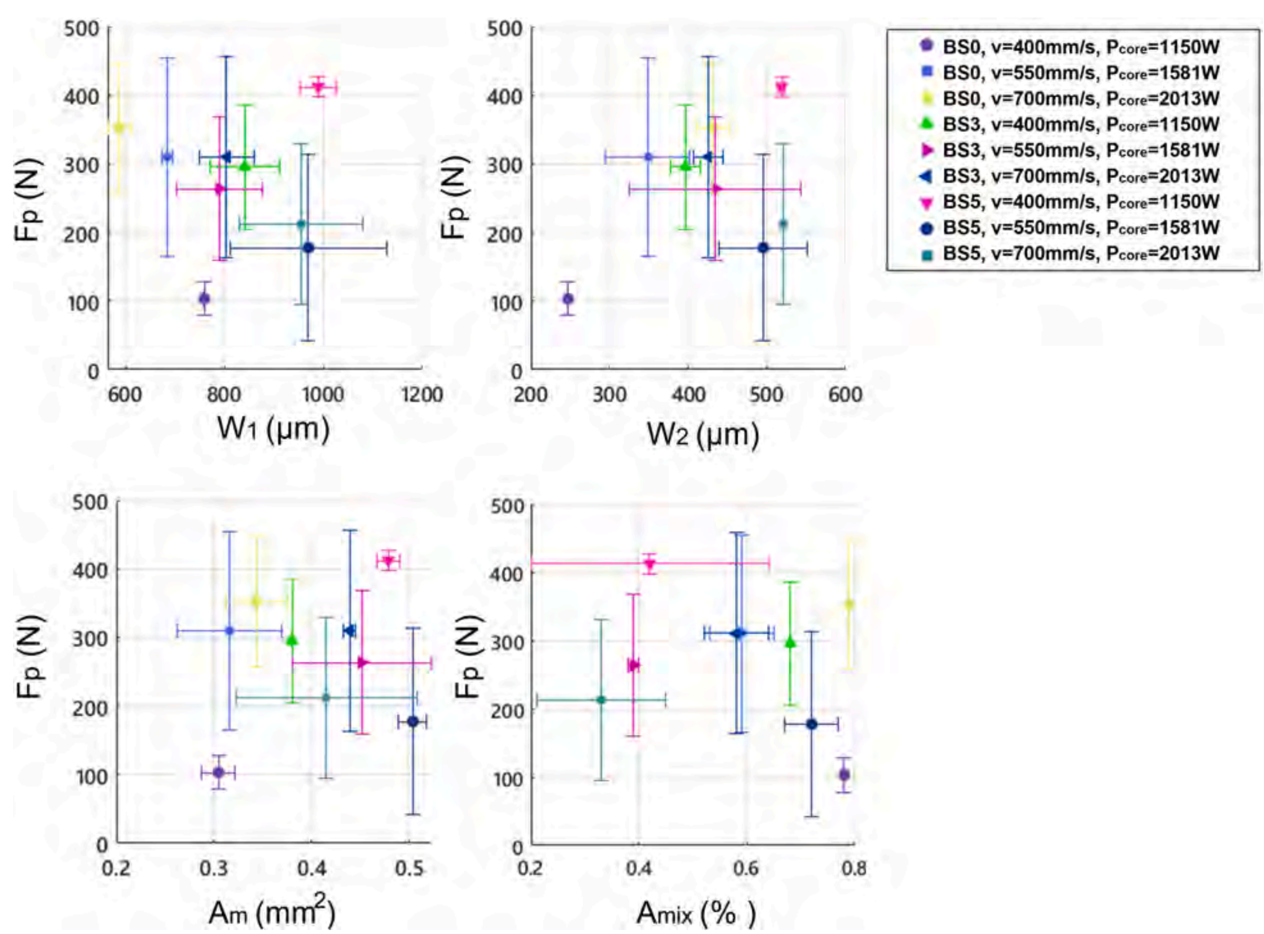

Fig. 16. The relationship between peak force at rupture and the weld section geometric parameters produced with with 2.88 J/mm energy per line.

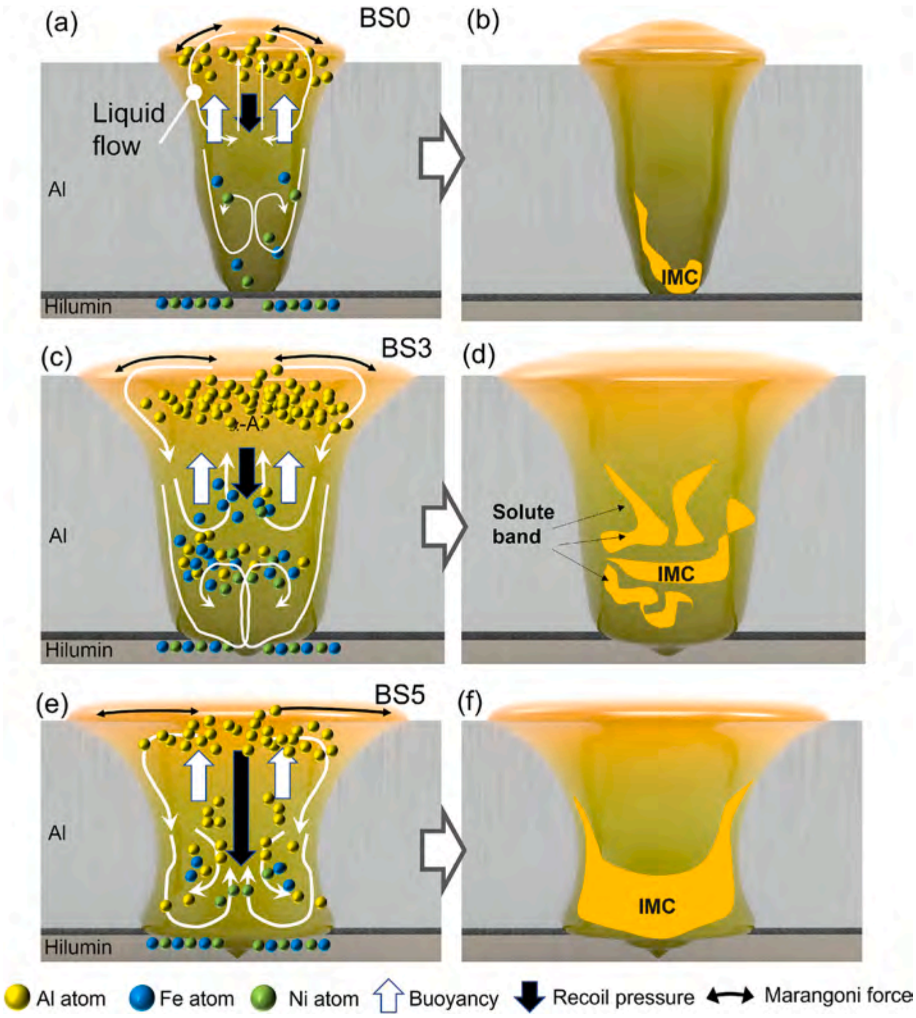

Fig. 17. Mechanism of IMC formation of melt pool in different BS conditions. (a) and (b) melt pool of BS0, (c) and (d) melt pool of BS3, (e) and (f) melt pool of BS5.

and phase transition in the melt pool under different BS conditions. As shown in Fig. 17(a), under BS0 conditions, due to the fact that most of the laser energy is focused on the core, the width of the melt pool is relatively small without the addition of rings, and the flow velocity inside the melt pool is relatively slow because of low heat input. The top of the melt pool is dominated by a large number of α-Al atoms (α-Al phase), but in the lower part, due to the melting of the Hilumin plate, some Fe and Ni atoms flow into the interior of the melt pool, resulting in IMC near the Al boundary. However, due to insufficient flow velocity and buoyancy inside the melt pool to allow Fe atoms to fully enter other areas of the melt pool and interact with each other, its IMC area is relatively small. As shown in Fig. 17(b), with the addition of the ring, in the LBW process of BS3, the laser heating radius increases, the melt pool gradually widens, the temperature gradient increases, and the Marangoni force gradually becomes dominant. Therefore, an accelerating flow driving force appears at the top of the melt pool, which promotes the interaction of different material atoms inside the melt pool [30]. The recoil pressure and buoyancy are roughly in equilibrium, and the IMC region is located in the lower part of the melt pool. Due to the continuous interaction of atoms, some solute bands are formed in the IMC, which is similar with the phenomenon in Fig. 14(b). Furthermore, as shown in Fig. 17(c), as the effect of ring addition becomes more significant, the melt pool width of BS5 is the largest and the internal fluidity is the strongest. However, the recoil pressure dominates at this time, breaking the internal flow direction and limiting the interaction area to the middle and lower layers of the melt pool. Therefore, there is no strip-shaped IMC generated, but a large area of IMC near the bonding area exists.

3.4.2. Electrical resistance

Because electrical resistance and A_{mix} are strongly correlated, changes in electrical resistance can roughly reflect the evolution of IMC morphology within LBW welds under different BS conditions. Different BS correspond to different IMC compositions, resulting in electrical resistance. Fig. 18 schematically illustrates how IMC morphology affects the current within the weld joint. For the thin IMC joint corresponding to BS0, as shown in Fig. 18(a), the joint filled with a thin IMC layer will exhibit lower electrical resistance [31]. This electrical resistance increase is primarily attributed to the formation of the Al_9FeNi phase on the Hilumin side [32]. Although IMC characterization results indicate that the IMC thickness is relatively thin, which generally facilitates current transfer [33]. However, low laser power can lead to inadequate weld connection as well. A mechanism diagram of the IMC joint corresponding to BS3 is shown in Fig. 18(b). Since the IMC exhibits mixed banding, the relatively large α-Al area could reduce electrical resistance and facilitates current transfer [34]. The IMC in the BS5 joint exhibits the largest area due to thorough mixing, as shown in Fig. 18(c). Furthermore, the higher content of the mixed phase on the Hilumin side significantly affects current transfer. In addition, weld inclusions and pores within the weld also affect resistance characteristics. In summary, achieving balanced fusion of dissimilar materials is key to improving joint electrical properties [32,34]. Limiting the formation of oversized

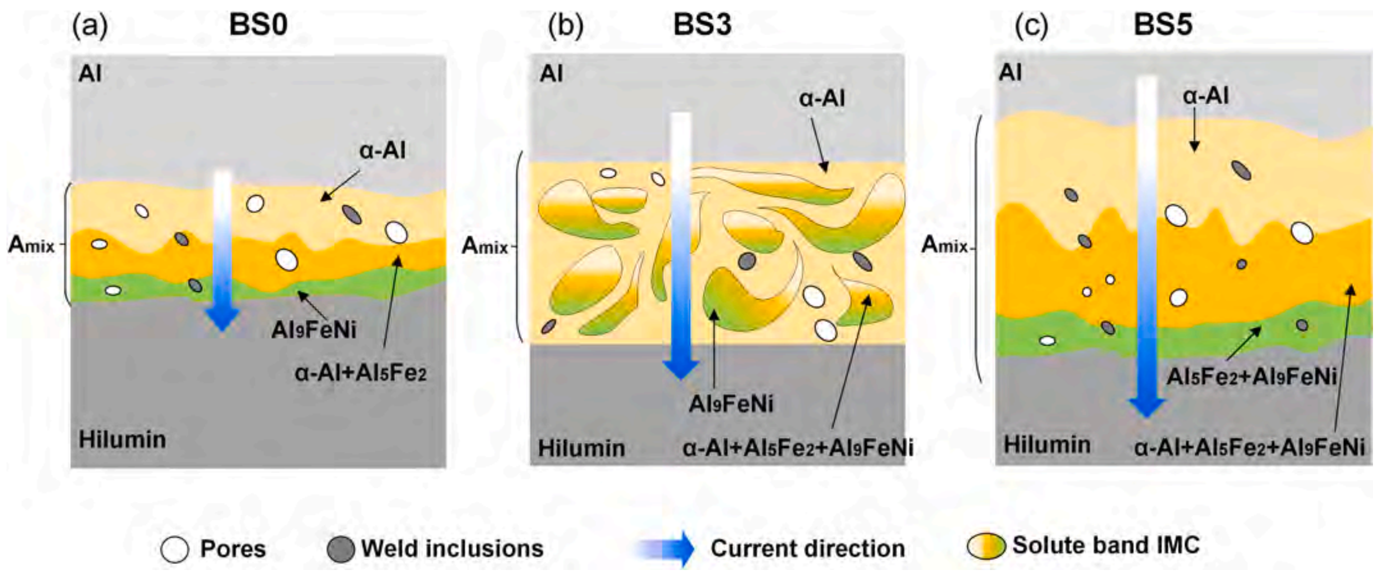

Fig. 18. Mechanism diagram of IMC impact on electrical resistance in different BS conditions. (a) IMC of BS0, (b) IMC of BS3, (b) IMC of BS5.

IMC and phase content variations on the Hilumin side is crucial for maintaining low electrical resistance.

3.4.3. Mechanical resistance

Fig. 19 shows SEM images of welded joints under different BS conditions and the corresponding IMC mechanism diagrams. As shown in Fig. 19(a), the weld corresponding to BS0 exhibits insufficient phase mixing due to the low heat input, resulting in a small IMC area [35,36]. Furthermore, the insufficient melt pool depth prevents the two materials from fully connecting in the region of the joint, leading to asymmetric crack propagation under tensile loading. These factors affect the mechanical properties of the weld. Fig. 19(b) shows the joint under BS3 and the IMC mechanism. Compared to BS0, the BS3 joint exhibits an adequate connection with no apparent lack of fusion. Areas susceptible to crack propagation appear on both sides of the joint interface. However, the increased content of the Ni mixed phase in the IMC and the larger A_{mix} contribute to improved mechanical strength [37]. With further increases in laser power, the joint corresponding to BS5 exhibits larger IMC zones, as shown in Fig. 19(c), with a further increase in the Ni mixed phase content, but also more pronounced crack growth areas appear on both sides of the joint.

In order to comprehensively compare the performance of the dissimilar LBW process, the peak force per unit length of the weld (laser weld strength, S_{lw}) is defined as a comparison index and compared with other current research results [24], as shown in Eq.(1). In order to avoid the differences caused by different process parameters, only the maximum value of S_{lw} is selected as the index.

$$S_{lw} = \frac{F_{Pm}}{L} \tag{1}$$

where F_{pm} is the maximum value of the average peak force in Fig. 13. L is the length of the circle weld bead. In this study, the S_{lw} is 32.9 N/mm. This result is similar to the existing related research result (S_{lw} is 31.8 N/mm [24]). Therefore, the battery pack connected by the LBW process proposed in this study has the characteristics of high performance.

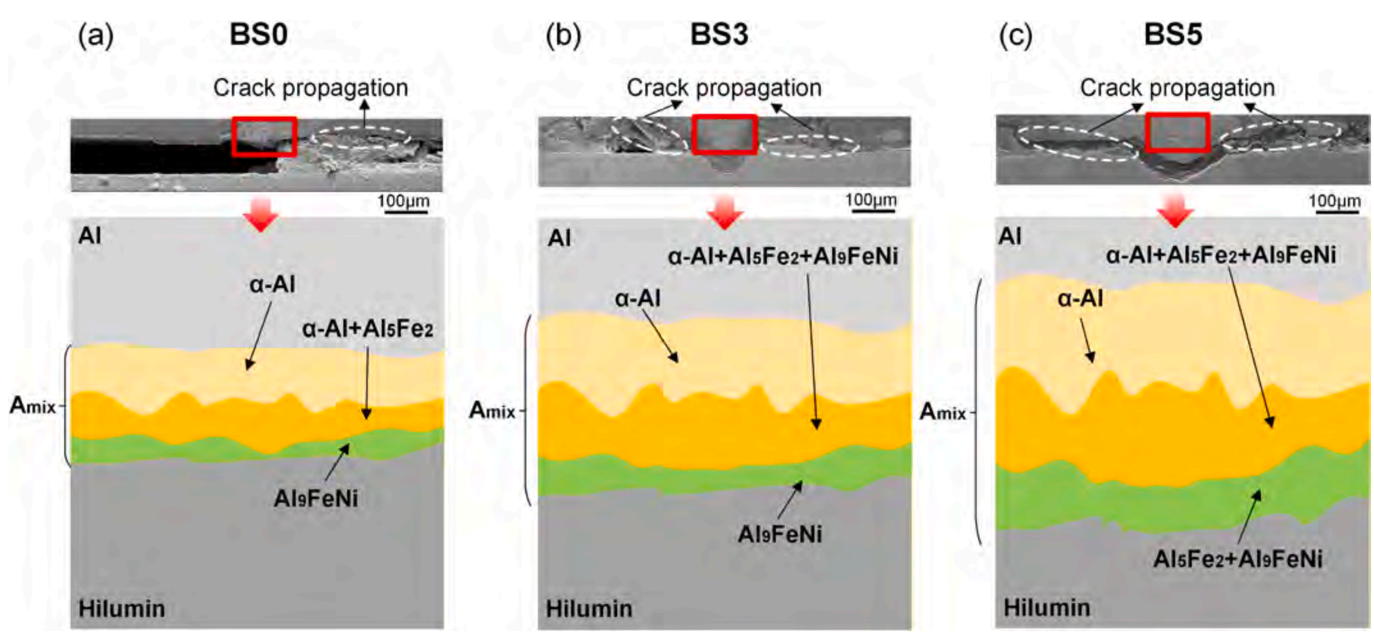

Fig. 19. Mechanism diagram of IMC impact on Mechanical resistance in different BS conditions. (a) IMC of BS0, (b) IMC of BS3, (b) IMC of BS5.

4. Conclusions

This study has investigated the influence laser beams on the weldability of aluminum alloy to Hilumin steel. The suitable selection of the BS is a key parameter to control metallurgical structure, mechanical and electrical properties. Moreover, the formation mechanism of IMC is explored as well. Main conclusions have been drawn as follow:

- The penetration of a weld is strongly linked with the P_{core}/v ratio. This is particularly important in experimentation of dissimilar material lap joints, as it allows to evaluate the difference in mixing of the two phases while keeping the amount of melted material at the interface constant. P_{core}/v ratio 2.88 J/mm is the suitable parameter for LBW dissimilar materials. Moreover, assessing this ratio allows the determination of an experimental plan with free parameters *v* and P_{ring} in which the process lies within the feasibility window.
- The variation in joint performance is strongly related to the formation and distribution of IMC within the weld bead. In particular, the presence of nickel is a fundamental element in this, due to its ability to refine the microstructure of the intermetallic phases, causing a considerable increase in the mechanical performances of the joint. Moreover, relative high nickel content can favour the formation of Al_9FeNi in substitution of Al_5Fe_2. Taking into consideration that the first composition shows significantly superior properties compared to the latter, also this aspect is believed to have a significant impact on joint performances. In addition, the changes in the temperature and force fields of the melt pool under different BS conditions have an important influence on the regional morphology of IMC.
- It was observed a compact distribution of IMC phases rich of nickel at the root of the weld. The peak force correlates positively with both A_{Hil} and A_{Al}, indicating that adequate fusion on both sides of the joint enhances mechanical performance. Meanwhile, electrical resistance shows a negative correlation with A_{Al} and a positive correlation with A_{mix}, suggesting that greater fusion on the aluminum side improves conductivity, while increased A_{mix} tends to impair it. A_{mix} has a greater impact on electrical resistance than on joint mechanical performance. Its correlation has increased by 80%. Overall, achieving a balanced fusion between A_{Hil} and A_{Al}, while limiting excessive A_{mix} formation, is essential for producing welds with both high strength and low resistance.

This study originates from the need to develop and manufacture a high-performance and efficient battery pack aimed for racing vehicles. Beyond this specific prototype application, the findings of this study have broader relevance for the design and production of advanced battery packs in various fields. In particular, the demonstrated feasibility of laser beam welding for dissimilar Al–Hilumin joints can be directly applied to lightweight EV battery modules, electric motorcycles, and next-generation passenger vehicles. Moreover, the insights into beam-shaping strategies and process optimization are valuable for large-scale battery pack manufacturing in electric buses and stationary energy storage systems, where high reliability and durability are critical. Future work will use advanced multiphysical simulations to better understand the mechanisms of phase change based on IMC and provide information about temperature/pressure fields and fluid-flow and help elucidate the impact of beam shaping on dissimilar laser welding.

CRediT authorship contribution statement

Tianqiu Xu: Writing – review & editing, Writing – original draft, Validation, Investigation, Formal analysis, Data curation. **Ali Gökhan Demir:** Writing – review & editing, Supervision, Methodology, Investigation, Funding acquisition, Conceptualization.

Declaration of competing interest

The authors declare that they have no known competing financial interests or personal relationships that could have appeared to influence the work reported in this paper.

Acknowledgements

The authors gratefully acknowledge the contribution of Mr. Paolo Cigarini and Mr. Simone D'Arcangelo in the experimental work. The authors would like to thank Optoprim for the longstanding collaboration. The authors express their gratidute to nLIGHT for the technical support. Tata Steel is acknowledged for the provided material.

Data availability

Data will be made available on request.

References

[1] B.F.A. da Silva, M.M. Kasaei, A. Akhavan-Safar, R.J.C. Carbas, E.A.S. Marques, L.F. M. da Silva, Fatigue analysis of novel hole hemmed joints for hybrid busbars in electric vehicle batteries, Eng. Fract. Mech. 311 (2024) 110590.

[2] A.G. Demir, J. Kriegler, A. Fortunato, L. Caprio, C. Geiger, L. Hille, M.K. Kick, A. Ascari, E. Liverani, M.F. Zaeh, Challenges and Opportunities for Laser applications in Electric Vehicle Manufacturing, in: L. Carrino, L.M. Galantucci, L. Settineri (Eds.), Selected Topics in Manufacturing: Emerging Trends from the Perspective of AITeM's Young Researchers, Springer Nature Switzerland, Cham, 2024, pp. 219–253.

[3] L. Zhao, J. Su, J. Li, Z. Abbas, H. Dai, L. Ma, Orthogonal experiments and bonding analysis of ultrasonic welded multi-layer battery foils and tabs, Eng. Sci. Technol. Int. J. 55 (2024) 101748.

[4] R. Schimanek, P. Bilge, F. Dietrich, Automated remanufacturing of lithium-ion batteries with shear separation, ultrasonic separation, and ultrasonic welding, Procedia CIRP 116 (2023) 227–232.

[5] X. Wei, J. Takahashi, K. Tatsumi, Resonant fatigue test performance of battery pack connections using wire bonding, Microelectron. Reliab. 168 (2025) 115705.

[6] M. Ank, T. Brehler, M. Lienkamp, Wire bond contact defect identification in battery modules of electric vehicles using pulses and differential voltage analysis, eTransportation 18 (2023) 100284.

[7] H. Kwon, U. Shah, X. Liu, T.J. Rinker, W. Cai, Ultrasonic-assisted resistance spot welding of multilayered Al foil stacks for Li-ion battery applications, J. Mater. Process. Technol. 317 (2023) 117990.

[8] M. Kogel-Hollacher, T. Nicolay, J. Reiser, S. Boley, J. Schwarz, G. Pallier, Beam shaping, process monitoring, and AI join forces for the benefit of e-mobility, high-power laser materials processing: applications, diagnostics, and systems XIV, SPIE (2025) 99–105.

[9] L. Caprio, B. Previtali, A.G. Demir, Effect of in-source beam shaping and laser beam oscillation on the electromechanical properties of Ni-plated steel joints for e-vehicle battery manufacturing, J. Laser Appl. 35 (4) (2023).

[10] M.C. Asirvatham, I. Masters, G. West, P. Haney, High-brightness laser welding with beam wobbling: achieving high-strength Al/Steel joints for battery busbars, J. Adv. Join. Processes 11 (2025) 100305.

[11] J. Fan, C. Thomy, F. Vollertsen, Effect of thermal cycle on the formation of intermetallic compounds in laser welding of aluminum-steel overlap joints, Phys. Procedia 12 (2011) 134–141.

[12] S.B. Halim, S. Bannour, K. Abderrazak, W. Kriaa, M. Autric, Numerical analysis of intermetallic compounds formed during laser welding of Aluminum-Magnesium dissimilar couple, Therm. Sci. Eng. Prog. 22 (2021) 100838.

[13] T. Li, D.-W. Zhou, Y.-r.-l. Yan, P. Peng, J.-S. Liu, First-principles and experimental investigations on ductility/brittleness of intermetallic compounds and joint properties in steel/aluminum laser welding, Trans. Nonferrous Met. Soc. Chin. 31 (10) (2021) 2962–2977.

[14] G.-Q. Liu, X.-D. Gao, C. Peng, X.-H. Liu, Y.-J. Huang, Y.-X. Zhang, D.-Y. You, Tensile resistance, microstructures of intermetallic compounds, and fracture modes of welded steel/aluminum joints produced using laser lap welding, Trans. Nonferrous Met. Soc. Chin. 30 (10) (2020) 2639–2649.

[15] J. Zhao, S. Geng, P. Jiang, M. Song, B. Xu, Q. Luo, Experimental and numerical research on formation mechanism of intermetallic compounds in laser brazing welding for Ti/Al dissimilar alloy, J. Mater. Res. Technol. 31 (2024) 2930–2944.

[16] S. Jabar, V.V. Pamarthi, Q. Hayat, M.H. Khan, H.R. Kotadia, P. Franciosa, A review of beam shaping approaches for near-infrared continuous-wave laser welding in e-mobility applications, Opt. Laser Technol. 192 (2025) 114000.

[17] X. Zhang, K. Xue, L. Liu, J. Xiao, J. Liu, F. Jin, M. Luo, M. Zhan, H. Li, Effect of electrical pulse treatment on the microstructural and mechanical responses of heterogeneous linear friction welded TC17/TC4 dissimilar joint, J. Mater. Res. Technol. 35 (2025) 1–12.

[18] Z. Long, H. Yongliang, D. Xuemei, L. Xin, Y. Limeng, C. Yuhua, X. Jilin, Formation mechanism of waveform interface in Mg/Al electromagnetic pulse welding, Mater. Today Commun. 45 (2025) 112401.

[19] Y. Zang, J. Xie, Y. Chen, M. Zheng, X. Liu, J. Shen, J.P. Oliveira, Resistance spot welded NiTi shape memory alloy to Ti6Al4V: correlation between joint microstructure, cracking and mechanical properties, Mater. Des. 253 (2025) 113859.

[20] K. Luo, Q. Fu, X. Liu, R. Zhao, Q. He, B. Hu, Z. An, W. Yang, Y. Zhang, S. Zhang, J. Zhan, J. Duan, Study of polarization transmission characteristics in nonspherical media, Opt. Lasers Eng. 174 (2024) 107970.

[21] X. Sun, Y. Xie, X. Meng, Z. Zhang, H. Tian, W. Dong, J. Dong, X. Ma, N. Wang, Y. Huang, Wire-based friction stir additive manufacturing of AZ31B magnesium alloy: precipitate behavior and mechanical properties, J. Magnesium Alloys (2025).

[22] M.C. Asirvatham, I. Masters, G. West, C. Harris, Influence of nickel-plating on laser weldability of aluminium busbars for lithium-ion battery interconnects, J. Mater. Res. Technol. 36 (2025) 4501–4515.

[23] A. Van Alboom, B. Lemmens, B. Breitbach, E. De Grave, S. Cottenier, K. Verbeken, Multi-method identification and characterization of the intermetallic surface layers of hot-dip Al-coated steel: FeAl3 or Fe4Al13 and Fe2Al5 or Fe2Al5+x, Surf. Coat. Technol. 324 (2017) 419–428.

[24] S. Jabar, T. Sun, P. Franciosa, H.R. Kotadia, D. Ceglarek, B. Paolini, R. Faulhaber, Effect of a ring-shaped laser beam on the weldability of aluminum-to-hilumin for battery tab connectors, J. Laser Appl. 35 (4) (2023).

[25] A. Körmöczi, G. Horváth, T. Szörényi, Z. Geretovszky, Laser soldering of nickel plated steel sheets, J. Laser Appl. 36 (1) (2024).

[26] L. Chen, R. Okawara, K. Matsuda, M. Nakao, K. Nagato, Effect of laser welding strategy for reducing intermetallic compound formation and residual stress, Precis. Eng. 88 (2024) 415–427.

[27] X.-M. Chen, X.-N. Wang, Q.-P. Dong, J.-M. Yu, Z. Zhu, H. Nagaumi, The effect of AlFeSi intermetallics compounds morphology on the corrosion behavior of Al–Mg–Si alloy laser welds, J. Mater. Res. Technol. 14 (2021) 1203–1207.

[28] S. Raja, F. Yusof, M.R. Muhamad, M.S. Mohd Mansor, A. Juri, B. Wu, M. F. Jamaludin, N. Ansari, J. Ren, Formation and influencing mechanism of the intermetallic compound in the friction stir welding of immiscible AZ31 and SPHC steel using aluminium powder as an additive, J. Mater. Res. Technol. 30 (2024) 9102–9114.

[29] A. Agarwal, S. D'Arcangelo, I. Poutiainen, A.G. Demir, Controlled mixing of Al and Cu in laser welded joints with combined use of core/ring beams and oscillation for EV battery pack applications, Opt. Laser Technol. 192 (2025) 113718.

[30] X. Wang, R.-H. Qiao, Y.-R. Zhang, J. Ma, C.-P. Liang, L.-J. Zhang, S.-J. Na, Study on element mixing of titanium-stainless steel dissimilar metal welding pool and its effect on joint properties in nanosecond laser welding, J. Mater. Process. Technol. 340 (2025) 118836.

[31] A. Piiroinen, A. Salminen, J. Pekkarinen, Investigation of resistance and intermetallic layer formation in laser-welded joints between copper and AM Aluminium for electrical connections, IOP Conf. Ser. Mater. Sci. Eng. IOP Publ. (2025) 012026.

[32] S. Sinhmar, S. Mandal, V.K. Yadav, K. Mondal, Investigation of corrosion and electrical resistance in laser welded Al-Cu joints for EV batteries, J. Storage Mater. 104 (2024) 114436.

[33] C. Jing, H. Mao, T. Xu, L. Pang, J. Lu, Z. Li, Z. Zhang, C. Liu, Fabrication strategy and mechanical behavior of large-size 316L stainless steel lattice structures via directed energy deposition-arc, Addit. Manuf. Front. (2026) 200296.

[34] S. Ali, J. Shin, Improvement in weld quality of Al and Cu joints using dual-beam laser welding, J. Manuf. Process. 119 (2024) 499–510.

[35] S. Kuryntsev, A. Review, Laser welding of dissimilar materials (Al/Fe, Al/Ti, Al/Cu)—methods and techniques, Microstruct. Prop. 15 (1) (2022) 122.

[36] M. Norouzian, M. Amne Elahi, P. Plapper, A review: suppression of the solidification cracks in the laser welding process by controlling the grain structure and chemical compositions, J. Adv. Join. Processes 7 (2023) 100139.

[37] S.R.A. Idris, N. Tamar Jaya, Exploring the barrier function of nickel in lead-free solder joints: thickness and aging effects on IMC formation, J. Phys. Conf. Ser. 2933 (1) (2025) 012003.